Journal of the Optical Society of America B
OPTICAL PHYSICS

Resonance enhanced absorption in a graphene monolayer using deep metal gratings

B. Zhao,[1] J. M. Zhao,[2] and Z. M. Zhang[1,*]

[1]George W. Woodruff School of Mechanical Engineering, Georgia Institute of Technology, Atlanta, Georgia, USA
[2]School of Energy Science and Engineering, Harbin Institute of Technology, Harbin, China
*Corresponding author: zhuomin.zhang@me.gatech.edu

Received 5 March 2015; revised 23 April 2015; accepted 23 April 2015; posted 29 April 2015 (Doc. ID 235705); published 19 May 2015

It has been demonstrated recently that metal gratings can significantly improve the near-infrared absorptance of graphene from 0.023 to nearly 0.70 because of the excitation of magnetic polaritons (MPs). In the present study, it is shown that the absorptance of graphene can be further enhanced to more than 0.80 by surface plasmon polaritons (SPPs) enabled by the grating. Meanwhile, graphene behaves as a sheet resistor that is able to boost the absorption when MPs or SPPs are excited without changing their resonance frequencies or dispersion relations. The effects of higher-order MPs, as well as the grating geometry on the enhanced absorptance, are also examined. Rigorous coupled-wave analysis (RCWA) is employed to calculate the radiative properties and power dissipation density in both the graphene and the metal grating. This study will facilitate the understanding of the coupling phenomena between graphene and nanostructures and may also benefit the design of next-generation graphene-based optical and optoelectronic devices.

OCIS codes: (160.4760) Optical properties; (050.0050) Diffraction and gratings; (240.5420) Polaritons; (240.6680) Surface plasmons.

http://dx.doi.org/10.1364/JOSAB.32.001176

1. INTRODUCTION

As a layered two-dimensional material with carbon atoms arranged in a honeycomb lattice, graphene has unique electrical, mechanical, and optical properties [1,2]. Unlike conventional metals, the electrons in graphene are massless quasi-particles (Dirac fermions), which exhibit a linear energy-momentum dispersion. Meanwhile, a remarkably high carrier mobility makes graphene a revolutionary material for optoelectronics related applications, such as ultrafast photodetectors, transparent electrodes, transistors, and biosensing [3–5]. In the visible and near-infrared (NIR) region, interband transitions can happen in doped graphene and the photons absorbed generate electron-hole pairs, creating electrical signals for photodetection. This makes graphene a potential material for the construction of an ultrafast photodetector, considering its high carrier mobility. However, because of its atomically thin thickness, the absorptance of graphene is only about 0.023 in this spectral region, and is related to the fine structure constant [6]. This minimal absorptance substantially hinders its applications in ultrafast optoelectronics; therefore, enhancing the absorption of graphene has drawn much attention recently.

The chemical potential of graphene can be changed through electrical gating or chemical doping and the optical properties of highly doped graphene resemble those of Drude-type materials in mid- to far-infrared region [7]. In this case, the graphene absorption can be improved by taking advantage of its plasmonic response and can be tuned by changing its chemical potentials [1,8]. One can make patterned graphene resonator and excite plasmons associated with them. For example, Thongrattanasiri *et al.* [9] demonstrated total light absorption by critical coupling in a single round-patterned sheet. Fang *et al.* [10] showed tunable enhanced absorption in a graphene nano-disk array from 0.03 to 0.30 by exciting local plasmonic resonances. Graphene can also be shaped to ribbons [11,12] to enhance its absorption since graphene surface plasmons can be excited in ribbons [13–15]. Graphene patch arrays of cross shapes [16] and square shapes [17] have also been demonstrated for absorption enhancement. In addition, graphene can be used together with other structures, such as gratings and photonic crystals to enhance its absorption [18–25]. For example, Gao *et al.* [26] and Zhan *et al.* [27] utilized a dielectric surface-relief grating to excite the surface plasmon wave in graphene, which also enhanced graphene absorption.

The above-mentioned plasmonic responses, however, cannot be excited in the visible and NIR region to enhance graphene absorption because the optical property of graphene is dominated by the interband transition. One way to enhance graphene absorption in this frequency region is to employ a microcavity that enables light to pass through the graphene sheet multiple times to improve the absorption of graphene

[4]. Another way is to utilize the plasmonic oscillations associated with optical nanoantennas that can create a localized strong electric field [28–33]. While the attenuated total reflection configuration setup can also be employed to enhance absorption near the critical angle [34], the enhancement is generally not very significant. It should be noted that guided resonances in dielectric gratings [35,36] can create an enhanced electric field to boost graphene absorption through critical coupling using photonic crystals [37], and may achieve total absorption. However, the enhancement achieved by this mechanism is usually narrowband and highly directionally sensitive. Recently, the present authors [38] proposed utilizing magnetic polaritons (MPs) in deep metal gratings to enhance absorptance of graphene and showed that up to near 0.70 absorptance in graphene can be obtained because of the enhanced electromagnetic field created when MPs are excited. However, the directional dependence as well as the effects of higher-order MPs and surface plasmon polaritons (SPPs) on graphene absorption have not been fully characterized.

In this work, absorption enhancement of graphene by SPPs and higher-order MPs in metal deep gratings is demonstrated numerically. The effect of the graphene on these resonances is illustrated by comparison of the dispersion relations of the gratings with and without graphene. The geometric effects on the absorption enhancement are also evaluated. The directional dependence of the absorption in graphene because of different types of resonance is elaborated. Local electric field and power dissipation density are depicted to further elucidate the underlying mechanisms. Detailed absorption profiles inside graphene are also presented at frequencies when resonance absorption occurs.

2. NUMERICAL MODELING

Figure 1 illustrates the structure of the graphene-covered deep gratings. The one-dimensional grating (extended to infinite in the y-direction) is made of silver (Ag) and the geometric parameters are period Λ, height h, and trench width b. When the plane of incidence is the x–z plane, the wavevector of an incident plane wave does not have a y-component and can be expressed as $\mathbf{k}_{\text{inc}} = k_x\hat{\mathbf{x}} + k_z\hat{\mathbf{z}} = k_0 \sin\theta\hat{\mathbf{x}} + k_0 \cos\theta\hat{\mathbf{z}}$, where θ is the incidence angle and k_0 is the wavevector in vacuum. For the one-dimensional grating considered here, since the wavevectors of all the diffracted waves lie in the x–z plane, the electromagnetic field is independent of y and no resonance excitation occurs in the y-direction. Here, the incident medium is assumed to be a vacuum or air (but with the same dielectric property as that of a vacuum). The graphene monoatomic layer lies at the top surface of the gratings at $z = 0$. Only transverse magnetic (TM) waves are considered in this study, since MPs and SPPs can only be excited when the magnetic field is in the y-direction for the one-dimensional grating shown in Fig. 1. The metal under the grating region is assumed to be sufficiently thick for it to be opaque. Therefore, the incoming radiation will be either reflected or absorbed, and the absorptance can be indirectly calculated from one minus the reflectivity.

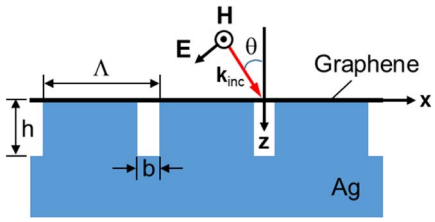

Fig. 1. Schematic of the graphene-covered one-dimensional grating nanostructure for a plane TM wave incident at an angle of θ. The top medium and the trench region are assumed to be a vacuum or air, and the bottom Ag region is assumed to be opaque or semi-infinite.

The rigorous coupled-wave analysis (RCWA) algorithm [39] is used to calculate the reflectivity of the structure as well as the field distribution, with sufficient Fourier expansion orders to ensure convergence. This algorithm has been tested for various geometric and materials configurations and is now available online as open source software [40]. In the simulation, the dielectric function of Ag, ε_{Ag}, is modeled with a simple Drude model [41,42], while graphene is modeled as an ultrathin layer with a thickness Δ according to an equivalent dielectric function [2]:

$$\varepsilon(\omega) = 1 + i\frac{\sigma_s}{\varepsilon_0\omega\Delta}, \tag{1}$$

where σ_s, ε_0, and ω are the sheet conductivity, the vacuum permittivity, and the angular frequency, respectively. Another method is to model graphene as a two-dimensional conductive film with a sheet conductivity σ_s, which induces a surface current along graphene and, thus, modifying the boundary conditions for the magnetic field. Those two methods yield identical results as long as Δ is chosen to be sufficiently small to ensure convergence [37,43]. In this study, graphene is treated as a thin film with an isotropic dielectric function so that the existing RCWA algorithm [40] can be directly employed without modifying the boundary conditions. In the calculation, $\Delta = 0.3$ nm is chosen to ensure convergence.

The sheet conductivity of graphene consists of the contribution from intraband (Drude-like term) and interband transitions, i.e., $\sigma_s = \sigma_D + \sigma_I$, respectively:

$$\sigma_D = \frac{i}{\omega + i/\tau}\frac{2e^2k_BT}{\pi\hbar^2}\ln\left[2\cosh\left(\frac{\mu}{2k_BT}\right)\right] \tag{2}$$

and

$$\sigma_I = \frac{e^2}{4\hbar}\left[G\left(\frac{\hbar\omega}{2}\right) + i\frac{4\hbar\omega}{\pi}\int_0^\infty \frac{G(\xi) - G(\hbar\omega/2)}{(\hbar\omega)^2 - 4\xi^2}\mathrm{d}\xi\right], \tag{3}$$

where $G(\xi) = \sinh(\xi/k_BT)/[\cosh(\mu/k_BT) + \cosh(\xi/k_BT)]$ [44]. Here, e is the electron charge, $\hbar$ is the reduced Planck constant, and k_B is the Boltzmann constant. The following parameters are used in all the calculations presented in this work: chemical potential $\mu = 0.3$ eV, relaxation time $\tau = 10^{-13}$ s, and temperature $T = 300$ K. With these parameters, $k_BT \ll \mu$ is satisfied, the interband contribution is manifested by a step function feature and the conductivity at photon energies above the threshold at $\hbar\omega \approx 2\mu$ is dominated by interband transitions [44]. This yields a purely real conductivity $\sigma_s = \sigma_I = e^2/4\hbar$ when photon energy is greater than 0.6 eV, which corresponds to a wavenumber of 4762 cm^{-1} (or wavelength of 2.1 μm). Since the frequency region of

interest in the present work is in the visible and near-infrared region, the conductivity of graphene is essentially a constant equal to $e^2/4\hbar$.

Conventionally, the absorptance obtained from one minus the reflectance calculated from RCWA is for the whole structure, which includes the graphene and the Ag grating. To separate how much power is indeed absorbed by the graphene only, one can first calculate the power dissipation density [45]:

$$w(x,z) = \frac{1}{2}\varepsilon_0\omega\varepsilon''(x,z)|\mathbf{E}(x,z)|^2, \tag{4}$$

in which $\mathbf{E}$ is the complex electric field [46], and ε'' is the imaginary part of the dielectric function. All properties are independent of y since the problem discussed here is two-dimensional. The calculation of power dissipation density is not part of the traditional RCWA algorithm, which only solves the radiative properties such as reflectance and transmittance. Nevertheless, the electromagnetic field in the structure can also be obtained from traditional RCWA [39]. Hence, Eq. (4) can be incorporated into the RCWA algorithm to calculate the local absorption [38,45,46]. The absorptance of graphene can then be obtained from the ratio of the power dissipated inside graphene over the incident power; hence [38],

$$\alpha = \frac{\iiint w(x,z)\mathrm{d}V}{\frac{1}{2}c_0\varepsilon_0|\mathbf{E}_{\mathrm{inc}}|^2 A\cos\theta}. \tag{5}$$

Here, the denominator is the power of the incident plane wave on an area A at incidence angle θ. For one-dimensional gratings, a unit length in the y direction can be used such that Eq. (5) is evaluated in the x–z plane. Moreover, the integration in the x direction needs to be performed only in one period. It can be seen from Eq. (1) that the imaginary part of the dielectric function of graphene can be expressed as $\varepsilon''(x,z) = \sigma_s/(\varepsilon_0\omega\Delta)$ since σ_s is purely real in this region. Meanwhile, the electric field inside the graphene layer is essentially independent of z. Therefore, the absorbed power in graphene can be expressed using its conductivity as follows:

$$\langle P_{\mathrm{abs}}\rangle = \int_{\mathrm{G}} w(x,z)\mathrm{d}V = \frac{\sigma_s}{2}\int_{-\Lambda/2}^{\Lambda/2}|E_x(x)|^2\mathrm{d}x. \tag{6}$$

Note that G indicates that the volume integration is carried out in graphene. The absorptance can be calculated by dividing Eq. (6) by the incident power.

One can apply the Cauchy–Schwarz inequality to Eq. (6):

$$\langle P_{\mathrm{abs}}\rangle \geq \frac{\sigma_s}{2\Lambda}\left|\int_{-\Lambda/2}^{\Lambda/2}E_x(x)\mathrm{d}x\right|^2. \tag{7}$$

The right-hand side (RHS) gives the lower bound of the power dissipated in graphene. If the electric field in graphene is independent of x, the RHS of Eq. (7) will be equal to the exact expression of $\langle P_{\mathrm{abs}}\rangle$. In this case, the electric field forms an alternating voltage across the graphene and the power dissipation directly resembles the macroscopic form, V_{RMS}^2/R. As to be shown in the next section, for MP resonances, the dissipation is concentrated only at the trench opening and the electric field across the trench can be approximated as uniform. The power dissipation can then be estimated by replacing the period Λ in the RHS of Eq. (7) with the trench width b [38].

3. RESULTS AND DISCUSSION

The absorptance of plain gratings and graphene-covered gratings is first presented for TM waves as a function of wavenumber (or frequency). The absorptance contours in terms of the wavenumber and the x-component of the wavevector are also depicted to reveal the directional dependence, as well as to delineate the MP and SPP dispersions. The geometric effects are also examined to illustrate the frequency tunability of the enhanced absorption. The local absorption (or dissipation) distributions are further examined to elucidate the effects of MPs and SPPs on the enhanced graphene absorption.

A. Absorptance of Plain and Graphene-Covered Gratings

The absorptance spectra for the plain and graphene-covered structure are shown in Fig. 2 for TM waves at incidence angle $\theta = 10°$ in terms of the wavenumber. The absorptance is for the whole structure and calculated from one minus the reflectance that is predicted by RCWA. In the simulation, the geometric parameters of the Ag grating are set to $\Lambda = 400$ nm, $b = 30$ nm, and $h = 200$ nm. These are the default values used in the present study unless otherwise specified. To realize a structure with such geometries, one could separately fabricate graphene using chemical vapor deposition on a copper foil and the grating structure by e-beam lithography with a lift-off process. Then, graphene could be transferred onto the grating to form the desired structure. There exist three distinct peaks in the absorptance spectra located at wavenumber $\nu =$ 6700 cm^{-1} 1.49 μm, 18350 cm^{-1} (545 nm), and 20930 cm^{-1} (478 nm). The value in parentheses indicates the corresponding wavelength. As will be explained later, these peaks are associated, respectively, with the excitation of the fundamental MP (MP1), the second-order MP (MP2), and an SPP. Clearly, adding graphene can increase the peak absorptance significantly without shifting the peak locations. For a plain grating, the absorptance is only 0.21 at MP1, because of the weak coupling between the two side walls of in the trench as noted previously [38,42]. Higher absorptance of 0.66 and 0.57 can be obtained with the MP2 and SPP modes,

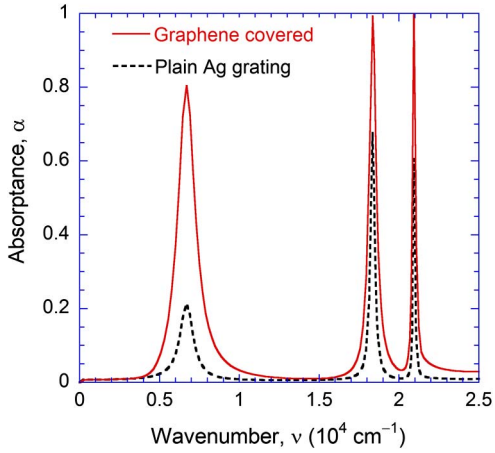

Fig. 2. Comparison of the absorptance of the graphene-covered and plain Ag grating with $h = 200$ nm, $\Lambda = 400$ nm, and $b = 30$ nm at incidence angle $\theta = 10°$ for TM waves.

respectively. With graphene coverage, the absorptance at the resonance wavenumbers is raised to 0.81, 0.99, and 1.0 for MP1, MP2, and SPP, respectively. However, the fraction of energy absorbed by the graphene monolayer itself is not the same as the difference between the absorptance of the whole structure before and after the graphene is added, since the absorption is redistributed because of the coupling effect to be discussed in Sections 3B and 3C.

The absorptance contours for the plain grating and graphene-covered grating are shown in Figs. 3(a) and 3(b), respectively, in the reduced zone scheme for $0 \le k_x \le \pi/\Lambda$. The lower-right corner beyond the light line is left blank since no propagating waves exist in a vacuum. The dispersion relations for different resonances, such as SPPs or MPs with different orders, are manifested by the bright bands. The incidence angle is related to the parallel wavevector component k_x by $k_x = 2\pi\nu \sin\theta$, and the inclined solid and dashed white lines represent $\theta = 10°$ and $\theta = 40°$, respectively. The contrast between Figs. 3(a) and 3(b) clearly shows that graphene enhances the absorption when resonances are excited for all the spectral region and incidence angles. The fundamental order, the second order, and the third order of MPs are excited in the considered spectral region as indicated by MP1, MP2, and MP3, respectively. MPs usually show up as nearly flat lines because the excitation is insensitive to the incidence angle [47]. Note that these modes are conventionally called waveguide modes, while MP is used here to stress the magnetic response of these resonances. SPP resonances and their effects on the radiative properties of gratings have been extensively investigated by many researchers [48–53]. The lower and upper branches can be identified as −1 and +1 orders of the SPP in the grating structures (as indicated in the contour above and below the sign "SPP"). The dots at the intersection of $\theta = 10°$ line and MP1, MP2, and SPP (−1 order) correspond to the three peaks in Fig. 2. Note that the anti-crossing between SPP and MPs can break the continuous bright bands [54] and thus neutralize the absorption peak. The anti-crossing effects also cause some hybridization between MP and SPP. The SPP bands show a discontinuity at $k_x = 0$, because two standing-wave solutions with different energies can be obtained, resulting in a bandgap [55,56].

In addition, the enhanced absorption can be tuned by the geometry of the grating. Figures 4(a) and 4(b) illustrate the grating height effect on the MP resonances for plain gratings and graphene-covered gratings, respectively. The MP excitation wavenumber decreases as h increases, and graphene enhances absorption without changing the resonance frequencies. While these figures are for normal incidence, similar results can be obtained for other incident directions. The MP resonance frequency can also be tuned by changing the slit width, and graphene also give rise to the absorptance without affecting the resonance frequency as demonstrated previously [38]. When the period increases (with fixed h and b), the MP resonance condition will not change much because of their localized resonance nature, whereas the SPP resonance will shift

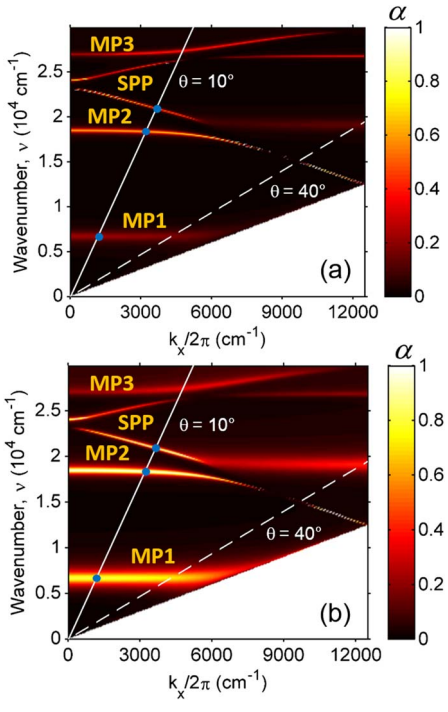

Fig. 3. Absorptance contours for (a) plain Ag grating and (b) graphene-covered grating. The white solid and dashed lines indicate the incidence at $\theta = 10°$ and $\theta = 40°$, respectively, and the intersections indicated by the dot markers correspond to the three absorption peaks shown in Fig. 2.

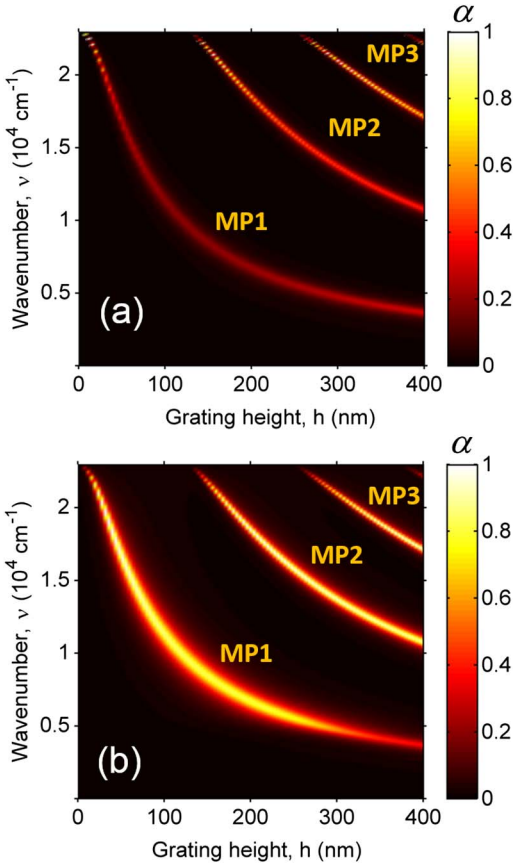

Fig. 4. Absorptance contours at normal incidence for the (a) plain and (b) graphene-covered Ag gratings in terms of the wavenumber and the grating height h.

to low frequencies [47]. Therefore, it is possible to tailor the grating geometries to enhance the absorption at the frequency of interest.

B. Enhanced Graphene Absorption by MPs

MPs represent the strong coupling between the magnetic resonance inside a micro/nanostructure and the external electromagnetic waves. The enhanced absorption at the MP excitation is directly related with the electromagnetic field at the resonance. The time-varying magnetic field parallel to the y-direction creates an oscillating closed current loop around the trench in the x–z plane, which generates a highly localized magnetic field inside the trench according to Lenz's law [50]. Figures 5(a) and 5(b) show electromagnetic fields for the MP1 and MP2 resonances, respectively, at $\theta = 10°$. The arrows show the electric field while the contour indicates the magnitude of the magnetic field, and the same pattern is followed in later field plots. The magnetic field inside the trench in Fig. 5(a) is enhanced by more than 12 times compared with the incidence, indicating the excitation of the fundamental mode of MP and showing the localization feature of the MP resonances [42].

Based on the profiles of the electromagnetic field and electric current, the resonance frequency for MP1 can be predicted by a suitable inductor-capacitor (LC) model as demonstrated for various structures [42,47,57,58]. For the plain grating considered here, the side and bottom walls of the trench serve as an inductor and the vacuum inside the trench and near the trench opening behaves as a capacitor. Since the conductivity of graphene is a real value as explained in the previous section, its impedance is also real and, thus, the overlaid graphene acts like a pure resistor in parallel with the capacitor and inductor; this explains why the resonance wavenumber is not affected by the graphene layer [38]. The same argument holds for higher-order MPs and SPPs. The electromagnetic field for MP2 as shown in Fig. 5(b) also exhibits the enhanced magnetic field with two antinodes in the trench region.

Not only is the magnetic field enhanced, but also the electric field is greatly enhanced at MP1 and MP2 resonances. The electric field is minimal in the Ag grating, except along the

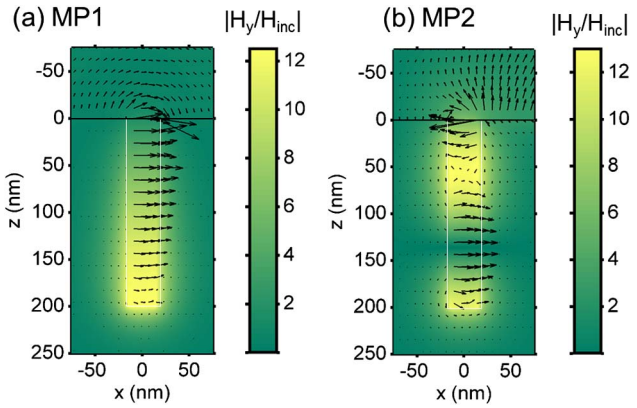

Fig. 5. Electromagnetic fields for (a) MP1 ($\nu = 6700\ \text{cm}^{-1}$) and (b) MP2 ($\nu = 18350\ \text{cm}^{-1}$) at $\theta = 10°$. The contour shows the normalized magnitude of the magnetic field, while the arrows indicate the direction and relative magnitude of the electric field.

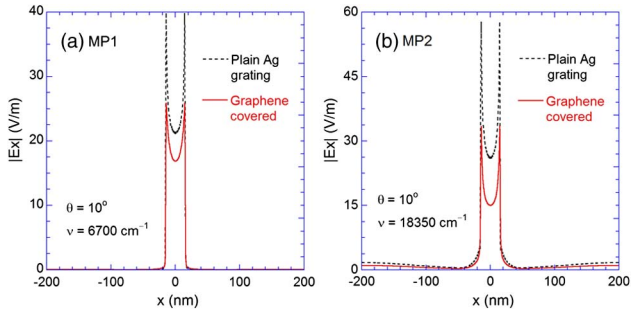

Fig. 6. Magnitude of the x-component of the electric field at $z = \Delta/2$ for plain and graphene-covered gratings at (a) MP1 ($\nu = 6700\ \text{cm}^{-1}$) and (b) MP2 ($\nu = 18350\ \text{cm}^{-1}$) resonances for $\theta = 10°$.

interface between Ag and vacuum, but is extremely strong in the trench especially at the trench opening as shown in Figs. 5(a) and 5(b). At the opening, the x-component of the electric field E_x dominates since the z-component is negligibly small. Figures 6(a) and 6(b) show E_x in the middle of graphene monolayer for MP1 and MP2, respectively. Note that the magnitude of the incident electric field is set to 1 V/m in the simulation. It can be seen that, for plain gratings, the electric field at the trench opening is enhanced by more than 20 times of the incident for MP1 and even higher for MP2. After covering graphene, the electric field is attenuated in both cases, and it can be inferred that adding graphene weakens the electric field. While Figs. 6(a) and 6(b) are calculated at $\theta = 10°$, the result for normal incidence [38] is almost identical. Note that for MP1, the electric field is negligibly small beyond the trench opening at $-15\ \text{nm} < x < 15\ \text{nm}$. The same cannot be said for MP2 for which the electric field is nontrivial beyond this range. This difference results in a different absorption profile in graphene as discussed in the following.

Figures 7(a) and 7(b) illustrate the power dissipation profiles calculated from Eq. (4) at MP1 resonance with $\theta = 10°$ for the plain grating and graphene-covered structure, respectively. For comparison, Figs. 7(c) and 7(d) show the power dissipation at MP2 resonance for the two structures. The contour describes the value of the power dissipation density and the same scalar bar is used for all four figures. The scale bar is not linear beyond $6 \times 10^5\ \text{W/m}^3$ to better show the absorption in grating. As shown in Figs. 7(a) and 7(c), the incoming radiation is mainly absorbed near the surfaces of the trench walls, especially at the corners. While displacement currents exist in a vacuum, it does not contribute to absorption since there is no dissipation. For MP2, the enhanced electric field induces extremely high power dissipation up to $10^6\ \text{W/m}^3$ at the four corners of the trench. After covering with graphene, however, the absorption by the grating is weakened for both resonance modes. It should be noted that the power dissipation inside graphene is extremely strong, reaching $10^8\ \text{W/m}^3$ for both MP1 and MP2. The shape of the power dissipation profile in graphene is similar to the electric field profile shown in Fig. 6, i.e., high in the trench opening with two spikes at the grating edges. A distinction between MP1 and MP2 is that the graphene absorption is

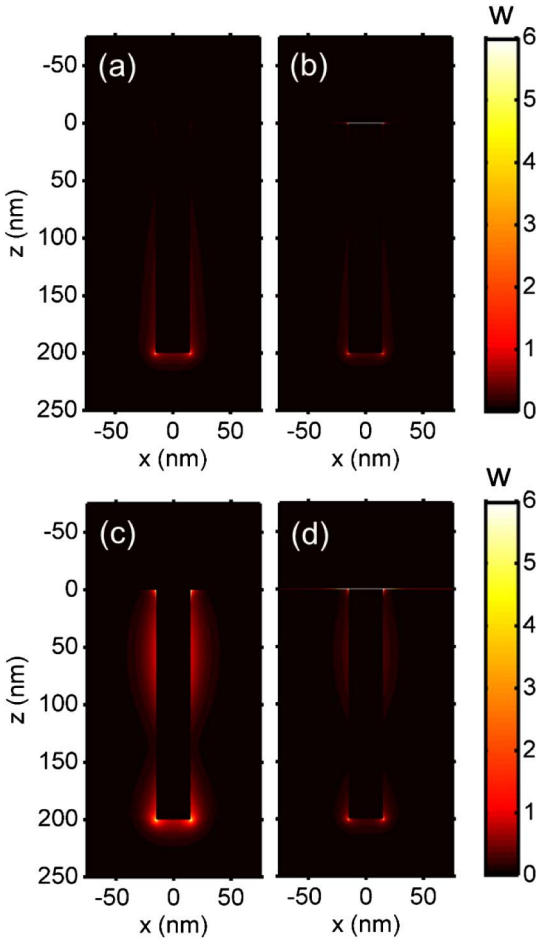

Fig. 7. Power dissipation profiles for the two structures when $\theta = 10°$: (a), (b) MP1 resonance ($\nu = 6700\ \mathrm{cm}^{-1}$) and (c), (d) MP2 resonance ($\nu = 18350\ \mathrm{cm}^{-1}$). The left (a), (c) are for the plain Ag grating and the right (b), (d) are for the graphene-covered grating. The unit of w is $10^5\ \mathrm{W/m^3}$ and the scale bar is not linear beyond $6 \times 10^5\ \mathrm{W/m^3}$.

negligibly small beyond $-15\ \mathrm{nm} < x < 15\ \mathrm{nm}$ for MP1, while absorption beyond this range may not be neglected for MP2.

The absorptance of graphene can be obtained by evaluating Eq. (6). For MP1, the dissipation of graphene is confined mainly in the range $-15\ \mathrm{nm} < x < 15\ \mathrm{nm}$, and the integration needs to be carried out in this region only. Furthermore, the lower bound absorptance of graphene can be obtained from the RHS of Eq. (7) by replacing the period Λ with the trench width b, which gives 0.66 as obtained previously [38]. The lower bound value agrees well with the exact value 0.68 for MP1. The integration of E_x from $-b/2$ to $b/2$ in the RHS of Eq. (7) can be viewed as the alternating voltage drop across the graphene, and b/σ_s is the resistance of graphene at the trench opening [38]. The graphene layer behaves like a resistor that dissipates power, resulting in a good agreement between the exact absorptance and the lower bound. Though the graphene layer is very thin, it carries an intense current that can induce a significant dissipation or loss. For MP2, the absorptance for the whole graphene is 0.77, among which 0.65 is in the trench opening and 0.12, resulting from the dissipation beyond the opening region because of the nontrivial electric field.

Table 1 compares the absorptance for plain gratings and graphene-covered gratings at different resonances. For graphene-covered gratings, the absorptance of graphene and grating is also listed separately. The absorptance of the grating is evaluated directly from Eq. (5) by performing the integration in the grating and the substrate. At MP2 resonance and $\theta = 10°$, the absorptance of the grating is 0.22 with graphene coverage. This is a significant reduction from that of 0.66 for a plain grating. On the other hand, the absorptance of graphene itself is boosted to 0.77, more than 33 times than 0.023 for a suspended graphene. Graphene can absorb more power than the Ag grating mainly because of two reasons. The first is that graphene is very lossy because of the interband transition. By assuming a thickness of 0.3 nm, the imaginary part of the effective dielectric function (ε'') for graphene is 6.6 at MP2 resonance, while $\varepsilon'' = 0.1$ for Ag at the same frequency. The second reason is that MP resonances create a strong electric field at the trench opening that is about 15 times that of the incidence waves, as shown in Fig. 6. Interestingly, the electric field strength remains the same through graphene in the z-direction. Although the electric field strength is comparable to that in graphene at the surface of the grating, it decays exponentially into the grating with a penetration depth of approximately 12 nm. Therefore, even though the thickness of graphene is 1,000 times smaller than that of the grating, the absorptance of graphene can be greater than that of the grating.

The graphene absorptance is nearly independent of θ for MP1 when θ is smaller than 20°, but will decrease at large angles closer to the light line. For example, at $\theta = 45°$, graphene absorptance decreases to 0.58, though not shown in the table. Moreover, the graphene absorptance at MP2 shows a decreasing trend as the incident angle increases, especially beyond 15° where the effect of anti-crossing between MP2 and SPP (−1 order) occurs. It should be noted that at long wavelengths (such as in the mid-infrared region), the imaginary part of σ_s becomes significant and the inductance of graphene can affect the MP resonance frequency [59]. Additional graphene plasmonic resonance features may also appear in the mid-infrared.

C. Enhanced Graphene Absorption by SPPs

As can be seen from Table 1, SPP results in nearly complete absorption by the graphene-covered grating structure, while both the resonance wavenumber and graphene absorptance are strongly angular dependent. The angular dependence of the resonance frequency can be understood by the negative slope of the −1 order SPP dispersion curve shown in Fig. 3. SPPs produce a longitudinal surface wave that propagates along the interface between the dielectric and the metal. Figure 8(a) shows the electromagnetic field for the plain grating at the SPP resonance at $\nu = 24050\ \mathrm{cm}^{-1}$ and for normal incidence. Note that the graphene-covered structure exhibits similar field distribution (not shown), except that the magnitude of the magnetic field is about half that for the plain grating. Strong electric field along the surface of the grating is generated as indicated by the arrows. It can be seen that the field strength exponentially decays away from the interface; this is a distinguished feature of

Table 1. Absorptance Calculated from RCWA at the Wavenumber Corresponding to the Resonance of Different Modes for Incidence Angle $\theta = 0°$ (Normal) and 10° with TM Waves[a]

	$\theta = 0°$			$\theta = 10°$		
	MP1	MP2	SPP	MP1	MP2	SPP
Resonance wavenumber ν(cm^{-1})	6700	18490	24050	6700	18350	20930
Plain grating	0.22	0.63	0.67	0.21	0.66	0.57
Graphene-covered structure	0.81	0.99	1.0	0.81	0.99	1.0
Graphene only	0.68	0.78	0.69	0.68	0.77	0.80
Grating only	0.13	0.21	0.31	0.13	0.22	0.20

[a]The last two rows list the individual absorptance of the graphene sheet and the grating in the graphene-covered structure.

SPPs. Meanwhile, the field along the surface of the grating shows a standing wave pattern with clear nodes and antinodes. At normal incidence, the incident photon can couple with two surface plasmons: one is the +1 order with a wavevector $k_{sp} = 2\pi/\Lambda$ (right traveling) and the other is the −1 order branch with $k_{sp} = -2\pi/\Lambda$ (left traveling). The two surface waves form a standing wave [55], whose wavelength is nearly equal to the period of the grating. Interestingly, there are some waveguide or MP features inside the deep trench or optical cavity when the SPP is excited. It can be seen from Fig. 8(a) that the field distribution inside the trench is similar to that of MP2 shown in Fig. 5(b). This implies the SPP resonance is not a pure SPP mode, but a hybridization of a standing surface wave and a localized resonance mode, which has been addressed in the literature for similar structures [51].

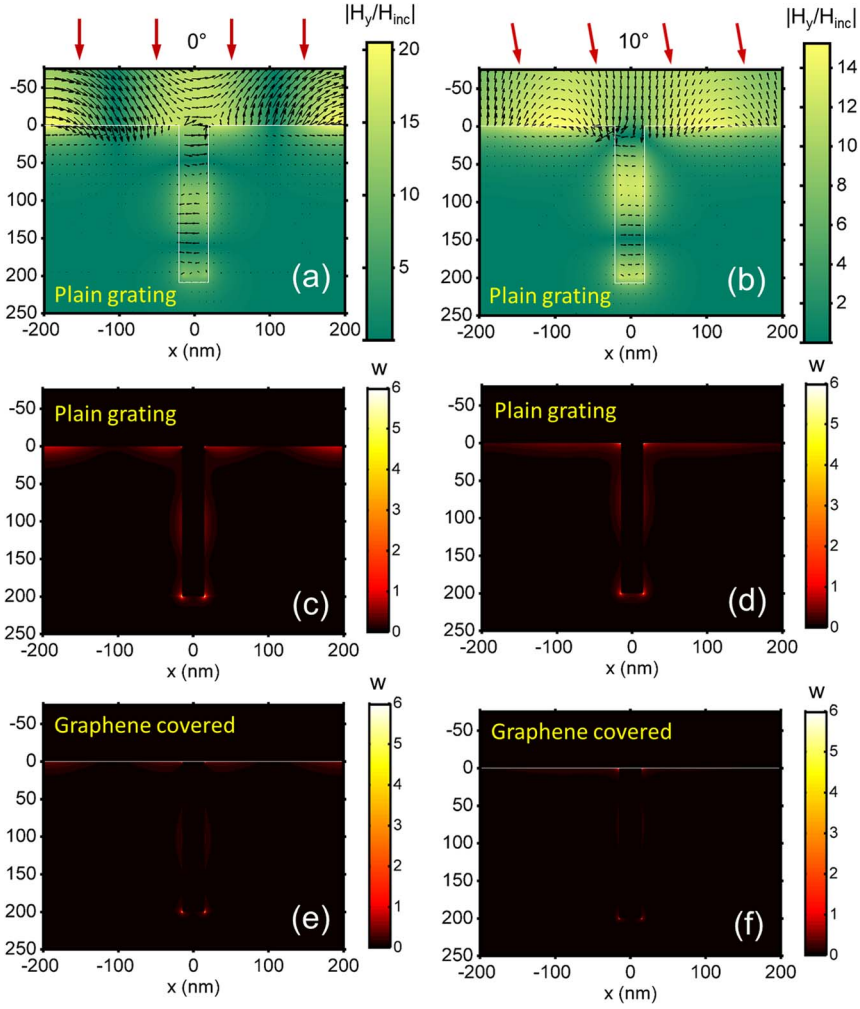

Fig. 8. (a), (b) Electromagnetic field distribution for plain grating, (c), (d) power dissipation contour for plain grating, and (e), (f) power dissipation contour for graphene-covered grating. The left figures (a), (c), (e) are for normal incidence at the SPP resonance $\nu = 24050$ cm^{-1} and the right figures (b), (d), (f) are for $\theta = 10°$ at the SPP resonance $\nu = 20930$ cm^{-1}. The unit of w is 10^5 W/m^3, and the scale is not linear beyond 6×10^5 W/m^3.

Figure 8(b) shows the field distribution of the plain grating at the SPP resonance and $\theta = 10°$, where the −1 order SPP is excited at $\nu = 24050\ \text{cm}^{-1}$. This resonance is actually a hybridization of a propagating surface wave (SPP) and a localized resonance (MP2). The magnetic field displays two antinodes in the trench, while standing waves appear along the grating surface. Furthermore, the left side has stronger field enhancement than the right side. Figures 8(c) and 8(d) show the power dissipation contours for the plain deep grating at normal and 10° incidence, respectively. The absorption along the surface of the grating in Fig. 8(c) shows a standing wave pattern with clear nodes and antinodes, which correspond to the magnetic field shown in Fig. 8(a). However, the standing wave feature does not present in Fig. 8(d). Meanwhile, on the two walls of the trench, the absorption contour is similar with that of MP2 shown in Fig. 7(c) for both normal and oblique incidence case because of the hybrid nature of the resonance.

Figures 8(e) and 8(f) depict the power dissipation contour for structures covered by graphene. They are similar to Figs. 8(c) and 8(d), but the absorption of grating is attenuated. Unlike in the case with MPs, the absorption of graphene for SPPs is significant not only in the trench opening but also along the surface of the grating (indicated by the bright white line). This is the reason why the absorptance distribution between graphene and grating is very sensitive to the incidence angle. For example, graphene has an absorptance of 0.69 at normal incidence and this value increases to 0.80 at $\theta = 10°$. It can be further boosted to 0.82 at $\theta = 14°$. The directional dependence can be attributed to the stronger electromagnetic field near the trench opening for oblique angles. The absorption at the grating surface beyond the trench appears not as strong in Fig. 8(c) as in Fig. 8(d), but is higher at the corners of the trench opening as indicated by the two brighter spots at the corners. Therefore, a stronger electric field is generated near the trench opening and the graphene is able to absorb more at oblique incidence than at normal incidence. However, when the incidence angle is greater than 20°, the absorption peak of SPPs becomes trivial because of anti-crossing and, thus, the graphene absorption because of SPPs becomes much weaker or may disappear at large angles.

To further understand graphene absorption at SPPs, the power dissipation along the center line of graphene at $z = \Delta/2$ is shown in Fig. 9. At normal incidence, the standing wave feature is clearly shown beyond the trench and the dissipation in the trench opening resembles the feature of MP2. Based on Eq. (5), the absorptance of graphene at the trench opening is 0.2, whereas the left portion ($-200\ \text{nm} < x < -15\ \text{nm}$) and right portion ($15\ \text{nm} < x < 200\ \text{nm}$) of graphene have the same absorptance of 0.245. Thus, the standing surface wave dominates the graphene absorption enhancement. At $\theta = 10°$, the absorption profile is no longer symmetric. The graphene at the trench opening absorbs 0.49 of the incoming power, while the left and right portion contributes to the absorptance by 0.18 and 0.13, respectively. Thus, the enhanced field near the trench opening is indeed the major contribution of the enhanced graphene absorption. Therefore, SPP resonance at oblique incidence can greatly enhance graphene absorption, even better than MPs, because of its hybrid nature.

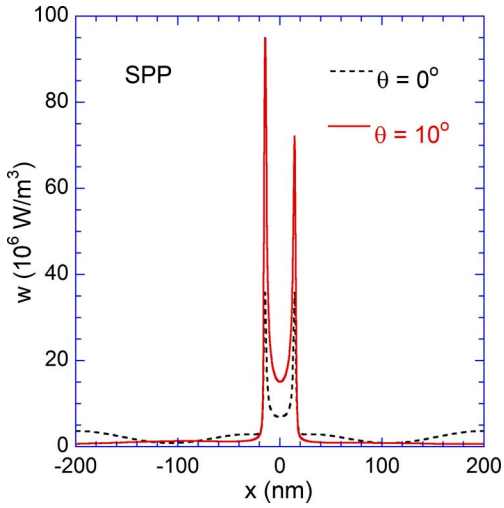

Fig. 9. Power dissipation density profile across the middle of the graphene layer when the SPP resonance is excited at normal incidence and $\theta = 10°$.

4. CONCLUSIONS

In this work, enhancement of graphene absorption by metal gratings is demonstrated theoretically. The excitation of MPs and SPP resonances can enhance the absorptance of graphene up to 0.80, without affecting the resonance frequency or dispersion in gratings. Because of the different nature of MP and SPP in the nanostructures, the enhanced graphene absorption is insensitive to the incidence angle for MPs when it is not close to the SPP dispersion line. In contrast, the SPP-enhanced graphene absorption depends strongly on the direction of incidence. The enhanced graphene absorption at MP resonances is localized at the trench opening. At the SPP resonance, however, surface waves contribute more to the enhancement at the normal incidence while the localized field near the trench opening contributes more at oblique angles. The understanding gained from this work may facilitate the development of graphene-based photodetecting, energy harvesting, as well as plasmonic devices.

National Science Foundation (NSF) (CBET-1235975); National Natural Science Foundation of China (NSFC) (No. 51421063).

BZ and ZMZ gratefully acknowledge the support by the National Science Foundation (NSF) (CBET-1235975). JMZ would like to thank the National Natural Science Foundation of China (NSFC) (No. 51421063) for their support.

REFERENCES

1. A. N. Grigorenko, M. Polini, and K. S. Novoselov, "Graphene plasmonics," Nat. Photonics **6**, 749–758 (2012).
2. A. Vakil and N. Engheta, "Transformation optics using graphene," Science **332**, 1291–1294 (2011).
3. F. Xia, T. Mueller, Y.-M. Lin, A. Valdes-Garcia, and P. Avouris, "Ultrafast graphene photodetector," Nat. Nanotechnol. **4**, 839–843 (2009).

4. M. Furchi, A. Urich, A. Pospischil, G. Lilley, K. Unterrainer, H. Detz, P. Klang, A. M. Andrews, W. Schrenk, G. Strasser, and T. Mueller, "Microcavity-integrated graphene photodetector," Nano Lett. **12**, 2773–2777 (2012).
5. J. Wu, M. Agrawal, H. A. Becerril, Z. Bao, Z. Liu, Y. Chen, and P. Peumans, "Organic light-emitting diodes on solution-processed graphene transparent electrodes," ACS Nano **4**, 43–48 (2010).
6. R. R. Nair, P. Blake, A. N. Grigorenko, K. S. Novoselov, T. J. Booth, T. Stauber, N. M. R. Peres, and A. K. Geim, "Fine structure constant defines visual transparency of graphene," Science **320**, 1308 (2008).
7. F. Wang, Y. Zhang, C. Tian, C. Girit, A. Zettl, M. Crommie, and Y. R. Shen, "Gate-variable optical transitions in graphene," Science **320**, 206–209 (2008).
8. D. N. Basov, M. M. Fogler, A. Lanzara, F. Wang, and Y. Zhang, "Colloquium: Graphene spectroscopy," Rev. Mod. Phys. **86**, 959–994 (2014).
9. S. Thongrattanasiri, F. H. L. Koppens, and F. J. García de Abajo, "Complete optical absorption in periodically patterned graphene," Phys. Rev. Lett. **108**, 047401 (2012).
10. Z. Fang, Y. Wang, A. E. Schlather, Z. Liu, P. M. Ajayan, F. J. García de Abajo, P. Nordlander, X. Zhu, and N. J. Halas, "Active tunable absorption enhancement with graphene nanodisk arrays," Nano Lett. **14**, 299–304 (2013).
11. V. V. Popov, T. Y. Bagaeva, T. Otsuji, and V. Ryzhii, "Oblique terahertz plasmons in graphene nanoribbon arrays," Phys. Rev. B **81**, 073404 (2010).
12. B. Liu, Y. Liu, and S. Shen, "Thermal plasmonic interconnects in graphene," Phys. Rev. B **90**, 195411 (2014).
13. A. Y. Nikitin, F. Guinea, F. J. Garcia-Vidal, and L. Martin-Moreno, "Surface plasmon enhanced absorption and suppressed transmission in periodic arrays of graphene ribbons," Phys. Rev. B **85**, 081405 (2012).
14. L. Ju, B. Geng, J. Horng, C. Girit, M. Martin, Z. Hao, H. A. Bechtel, X. Liang, A. Zettl, Y. R. Shen, and F. Wang, "Graphene plasmonics for tunable terahertz metamaterials," Nat. Nanotechnol. **6**, 630–634 (2011).
15. M. S. Jang, V. W. Brar, M. C. Sherrott, J. J. Lopez, L. Kim, S. Kim, M. Choi, and H. A. Atwater, "Tunable large resonant absorption in a midinfrared graphene salisbury screen," Phys. Rev. B **90**, 165409 (2014).
16. A. Fallahi and J. Perruisseau-Carrier, "Design of tunable biperiodic graphene metasurfaces," Phys. Rev. B **86**, 195408 (2012).
17. A. Andryieuski and A. V. Lavrinenko, "Graphene metamaterials based tunable terahertz absorber: effective surface conductivity approach," Opt. Express **21**, 9144–9155 (2013).
18. J.-T. Liu, N.-H. Liu, L. Wang, X.-H. Deng, and F.-H. Su, "Gate-tunable nearly total absorption in graphene with resonant metal back reflector," Europhys. Lett. **104**, 57002 (2013).
19. H. Yuan, H. Yang, P. Liu, X. Jiang, and X. Sun, "Mode manipulation and near-THz absorptions in binary grating-graphene layer structures," Nanoscale Res. Lett. **9**, 90 (2014).
20. T. M. Slipchenko, M. L. Nesterov, L. Martin-Moreno, and A. Y. Nikitin, "Analytical solution for the diffraction of an electromagnetic wave by a graphene grating," J. Opt. **15**, 114008 (2013).
21. B.-Z. Xu, C.-Q. Gu, Z. Li, and Z.-Y. Niu, "A novel structure for tunable terahertz absorber based on graphene," Opt. Express **21**, 23803–23811 (2013).
22. Y. Zhang, Y. Feng, B. Zhu, J. Zhao, and T. Jiang, "Graphene based tunable metamaterial absorber and polarization modulation in terahertz frequency," Opt. Express **22**, 22743–22752 (2014).
23. X. Ying, Y. Pu, Z. Li, Z. Liu, and Y. Jiang, "Absorption enhancement of graphene salisbury screen in the mid-infrared regime," J. Opt. **44**, 1–9 (2014).
24. R. Alaee, M. Farhat, C. Rockstuhl, and F. Lederer, "A perfect absorber made of a graphene micro-ribbon metamaterial," Opt. Express **20**, 28017–28024 (2012).
25. N. M. R. Peres and V. B. Yu, "Enhancing the absorption of graphene in the terahertz range," Europhys. Lett. **101**, 58002 (2013).
26. W. Gao, J. Shu, C. Qiu, and Q. Xu, "Excitation of plasmonic waves in graphene by guided-mode resonances," ACS Nano **6**, 7806–7813 (2012).
27. T. R. Zhan, F. Y. Zhao, X. H. Hu, X. H. Liu, and J. Zi, "Band structure of plasmons and optical absorption enhancement in graphene on subwavelength dielectric gratings at infrared frequencies," Phys. Rev. B **86**, 165416 (2012).
28. Z. Fang, Z. Liu, Y. Wang, P. M. Ajayan, P. Nordlander, and N. J. Halas, "Graphene-antenna sandwich photodetector," Nano Lett. **12**, 3808–3813 (2012).
29. Y. Yao, R. Shankar, P. Rauter, Y. Song, J. Kong, M. Loncar, and F. Capasso, "High-responsivity mid-infrared graphene detectors with antenna-enhanced photocarrier generation and collection," Nano Lett. **14**, 3749–3754 (2014).
30. T. Stauber, G. Gómez-Santos, and F. J. G. de Abajo, "Extraordinary absorption of decorated undoped graphene," Phys. Rev. Lett. **112**, 077401 (2014).
31. T. J. Echtermeyer, L. Britnell, P. K. Jasnos, A. Lombardo, R. V. Gorbachev, A. N. Grigorenko, A. K. Geim, A. C. Ferrari, and K. S. Novoselov, "Strong plasmonic enhancement of photovoltage in graphene," Nat. Commun. **2**, 458 (2011).
32. M. Hashemi, M. H. Farzad, N. A. Mortensen, and S. Xiao, "Enhanced absorption of graphene in the visible region by use of plasmonic nanostructures," J. Opt. **15**, 055003 (2013).
33. Y. Yao, M. A. Kats, R. Shankar, Y. Song, J. Kong, M. Loncar, and F. Capasso, "Wide wavelength tuning of optical antennas on graphene with nanosecond response time," Nano Lett. **14**, 214–219 (2013).
34. W. Zhao, K. Shi, and Z. Lu, "Greatly enhanced ultrabroadband light absorption by monolayer graphene," Opt. Lett. **38**, 4342–4345 (2013).
35. M. Grande, M. A. Vincenti, T. Stomeo, G. V. Bianco, D. de Ceglia, N. Aközbek, V. Petruzzelli, G. Bruno, M. De Vittorio, M. Scalora, and A. D'Orazio, "Graphene-based absorber exploiting guided mode resonances in one-dimensional gratings," Opt. Express **22**, 31511–31519 (2014).
36. J.-H. Hu, Y.-Q. Huang, X.-F. Duan, Q. Wang, X. Zhang, J. Wang, and X.-M. Ren, "Enhanced absorption of graphene strips with a multilayer subwavelength grating structure," Appl. Phys. Lett. **105**, 221113 (2014).
37. J. R. Piper and S. Fan, "Total absorption in a graphene monolayer in the optical regime by critical coupling with a photonic crystal guided resonance," ACS Photonics **1**, 347–353 (2014).
38. B. Zhao, J. M. Zhao, and Z. M. Zhang, "Enhancement of near-infrared absorption in graphene with metal gratings," Appl. Phys. Lett. **105**, 031905 (2014).
39. B. J. Lee, Y. B. Chen, and Z. M. Zhang, "Transmission enhancement through nanoscale metallic slit arrays from the visible to mid-infrared," J. Comput. Theor. Nanosci. **5**, 201–213 (2008).
40. http://zhang-nano.gatech.edu/.
41. Z. M. Zhang, *Nano/Microscale Heat Transfer* (McGraw-Hill, 2007).
42. B. Zhao and Z. M. Zhang, "Study of magnetic polaritons in deep gratings for thermal emission control," J. Quant. Spectrosc. Radiat. Transfer **135**, 81–89 (2014).
43. M. Lim, S. S. Lee, and B. J. Lee, "Near-field thermal radiation between graphene-covered doped silicon plates," Opt. Express **21**, 22173–22185 (2013).
44. L. A. Falkovsky, "Optical properties of graphene," J. Phys. Conf. Ser. **129**, 012004 (2008).
45. J. M. Zhao and Z. M. Zhang, "Electromagnetic energy storage and power dissipation in nanostructures," J. Quant. Spectrosc. Radiat. Transfer **151**, 49–57 (2015).
46. K.-H. Brenner, "Aspects for calculating local absorption with the rigorous coupled-wave method," Opt. Express **18**, 10369–10376 (2010).
47. L. P. Wang and Z. M. Zhang, "Resonance transmission or absorption in deep gratings explained by magnetic polaritons," Appl. Phys. Lett. **95**, 111904 (2009).
48. F. Marquier, M. Laroche, R. Carminati, and J. J. Greffet, "Anisotropic polarized emission of a doped silicon lamellar grating," J. Heat Transfer **129**, 11–16 (2007).
49. N. Nguyen-Huu, Y.-B. Chen, and Y.-L. Lo, "Development of a polarization-insensitive thermophotovoltaic emitter with a binary grating," Opt. Express **20**, 5882–5890 (2012).

50. B. Zhao, L. Wang, Y. Shuai, and Z. M. Zhang, "Thermophotovoltaic emitters based on a two-dimensional grating/thin-film nanostructure," Int. J. Heat Mass Transfer **67**, 637–645 (2013).
51. F. J. Garcia-Vidal, J. Sanchez-Dehesa, A. Dechelette, E. Bustarret, T. Lopez-Rios, T. Fournier, and B. Pannetier, "Localized surface plasmons in lamellar metallic gratings," J. Lightwave Technol. **17**, 2191–2195 (1999).
52. T. López-Rios, D. Mendoza, F. J. García-Vidal, J. Sánchez-Dehesa, and B. Pannetier, "Surface shape resonances in lamellar metallic gratings," Phys. Rev. Lett. **81**, 665–668 (1998).
53. J. A. Porto, F. J. García-Vidal, and J. B. Pendry, "Transmission resonances on metallic gratings with very narrow slits," Phys. Rev. Lett. **83**, 2845–2848 (1999).
54. J. X. Chen, P. Wang, Z. M. Zhang, Y. Lu, and H. Ming, "Coupling between gap plasmon polariton and magnetic polariton in a metallic-dielectric multilayer structure," Phys. Rev. E **84**, 026603 (2011).
55. W. L. Barnes, T. W. Preist, S. C. Kitson, and J. R. Sambles, "Physical origin of photonic energy gaps in the propagation of surface plasmons on gratings," Phys. Rev. B **54**, 6227–6244 (1996).
56. W. L. Barnes, A. Dereux, and T. W. Ebbesen, "Surface plasmon subwavelength optics," Nature **424**, 824–830 (2003).
57. R. Feng, J. Qiu, L. H. Liu, W. Ding, and L. Chen, "Parallel LC circuit model for multi-band absorption and preliminary design of radiative cooling," Opt. Express **22**, A1713–A1724 (2014).
58. A. Sakurai, B. Zhao, and Z. M. Zhang, "Resonant frequency and bandwidth of metamaterial emitters and absorbers predicted by an RLC circuit model," J. Quant. Spectrosc. Radiat. Transfer **149**, 33–40 (2014).
59. H. Wang, Y. Yang, and L. P. Wang, "Infrared frequency-tunable coherent thermal sources," J. Opt. **17**, 045104 (2015).